

Hand-powered microfluidics: A membrane pump with a patient-to-chip syringe interface

Max M. Gong,^{1,a)} Brendan D. MacDonald,^{1,a)} Trung Vu Nguyen,^{2,3,4} and David Sinton^{1,b)}

¹*Department of Mechanical and Industrial Engineering, University of Toronto, 5 King's College Road, Toronto, Ontario M5S 3G8, Canada*

²*Clinical Laboratories, National Hospital for Tropical Diseases, 78 Giai Phong Street, Hanoi, Vietnam*

³*Department of Microbiology, Hanoi Medical University, 1 Ton That Tung Street, Hanoi, Vietnam*

⁴*Department of Clinical Microbiology and Parasitology, Hanoi Medical University, 1 Ton That Tung Street, Hanoi, Vietnam*

(Received 28 August 2012; accepted 5 October 2012; published online 19 October 2012)

In this paper, we present an on-chip hand-powered membrane pump using a robust patient-to-chip syringe interface. This approach enables safe sample collection, sample containment, integrated sharps disposal, high sample volume capacity, and controlled downstream flow with no electrical power requirements. Sample is manually injected into the device via a syringe and needle. The membrane pump inflates upon injection and subsequently deflates, delivering fluid to downstream components in a controlled manner. The device is fabricated from poly(methyl methacrylate) (PMMA) and silicone, using CO₂ laser micromachining, with a total material cost of ~0.20 USD/device. We experimentally demonstrate pump performance for both deionized (DI) water and undiluted, anticoagulated mouse whole blood, and characterize the behavior with reference to a resistor-capacitor electrical circuit analogy. Downstream output of the membrane pump is regulated, and scaled, by connecting multiple pumps in parallel. In contrast to existing on-chip pumping mechanisms that typically have low volume capacity (~5 μ L) and sample volume throughput (~1–10 μ L/min), the membrane pump offers high volume capacity (up to 240 μ L) and sample volume throughput (up to 125 μ L/min).

© 2012 American Institute of Physics. [<http://dx.doi.org/10.1063/1.4762851>]

I. INTRODUCTION

Fluid transport and flow control components, such as pumps, are required front-end components of lab-on-a-chip devices for the delivery and control of biological samples.¹ A range of micropumps have been developed for biomedical applications based on electrostatic,² piezoelectric,^{3–5} electromagnetic,^{6,7} electroosmotic,⁸ and pneumatic⁹ actuations. Although these pumping mechanisms provide precise flow rates,¹⁰ they require electrical control and external electrical or air supply.

In the context of point-of-care diagnostics, electrically and pneumatically actuated pumps are not well-suited due to the requirement of external support equipment (e.g., a power or air supply). Point-of-care diagnostic devices must be low cost, portable, robust, and minimally instrumented, especially if they are to be deployed for public health in resource-poor, remote, or developing settings.^{11,12} In these settings, energy and material resources are often limited or too costly to acquire. The ideal strategy, then, is to integrate point-of-care diagnostic devices with on-chip pumping mechanisms that can leverage battery power¹³ or human-power^{14–16} and eliminate the necessity of external support equipment.

^{a)}M. M. Gong and B. D. MacDonald contributed equally to this work.

^{b)}Author to whom correspondence should be addressed. Electronic mail: sinton@mie.utoronto.ca.

A number of on-chip pumping mechanisms have shown promise for point-of-care applications. Walker and Beebe¹⁷ presented a passive pumping method based on the surface tension of a small droplet of liquid. Droplets of water were pipetted into open inlet and outlet ports with the inlet droplet having a larger curvature. The difference in capillary pressure induced flow in the channel.¹⁸ Gervais and Delamarche¹⁹ demonstrated an integrated, one-step immunoassay that used a capillary pump for transport of blood serum. The capillary pump, placed at the end of the device, induced a negative capillary pressure to allow continuous flow of sample volume from an open reservoir. In another integrated immunodiagnostic device, Dimov *et al.*²⁰ used vacuum pressure to deliver a few microliters of whole blood from open ports to downstream analysis. They exploited the high gas-permeability of poly(dimethylsiloxane) (PDMS) to remove the trapped air within dead-ended channels. Similarly, Li *et al.*²¹ developed a “place n play” modular pump based on the degassed-PDMS approach. Weibel *et al.*²² also leveraged the properties of PDMS for storing and pumping fluids. PDMS compartments were deformed under fluid pressure and closed off by manual screw valves on the upstream and downstream sides. The isolated sample could be used later by opening the downstream screw valve. Chin *et al.*¹⁴ used a syringe attached to an on-chip port via a metal spacer to induce negative vacuum pressure for transporting whole blood through an immunoassay. In a similar manner, Wu *et al.*¹⁶ employed an air-filled hand-held syringe as a portable plastic pump for on-chip continuous-flow polymerase chain reaction (PCR). The air-filled syringe was connected to a continuous-flow PCR component via highly gas-permeable tubing. The flow of a sample plug was enabled by a pressure gradient created by the compressed air in the syringe and air escaping from the tubing. Another more recently developed hand-operated pump is the squeeze-chip by Li *et al.*¹⁵ In their device, fluid transport is dictated by finger-operated PDMS reservoirs with a network of check valves. When an operator presses on a reservoir, valves open and close to allow fluid movement downstream and refilling of the sample reservoir from an open port. These existing on-chip pumping mechanisms have addressed some important challenges in the design of pumps for point-of-care applications, such as low cost, portability, and minimal instrumentation. However, several key attributes are still lacking: (1) a robust patient-to-chip interface for safe sample collection that leverages established sample collection methods (e.g., syringe and needle), (2) biological sample containment to avoid exposure of the operator and/or environment to infectious agents, and to ensure sample integrity, and (3) capacity for high sample volume throughput.

In this paper, we present a device that incorporates an on-chip hand-powered membrane pump leveraging established syringe-based sample collection methods. This approach enables safe sample collection, sample containment, integrated sharps disposal, high sample volume capacity, and controlled downstream flow with no electrical power requirements. The working principle and design of the device are described, and the fabrication of the membrane pump is also presented. Furthermore, the performance of the pump is established through experiments and characterized using an electrical circuit analogy.

II. WORKING PRINCIPLE AND DESIGN

The device is comprised of several interconnected components for collecting and transporting fluids: a patient-to-chip syringe interface, membrane pump, fluidic resistor, and downstream component, as shown in Fig. 1. The patient-to-chip syringe interface exploits existing sample collection methods (e.g., syringe and needle) to safely collect patient blood (or other bodily fluids) into the device. An operator injects the patient sample into the device by inserting the needle into the syringe interface. To reduce the risk of operator injury, the device should be braced against a solid surface such that only one hand is used for needle insertion. The injected patient sample is contained within the membrane pump, which deforms under the fluid pressure. The membrane pump stores the sample volume and the mechanical energy of the operator as it inflates. Subsequent deflation of the pump pushes the sample downstream, as regulated through a fluidic resistor.

A typical human thumb can apply a force of 70 N²³ resulting in an injection pressure of 4 MPa for a 1 ml BD plastic syringe. The potential for such high levels of operator-generated

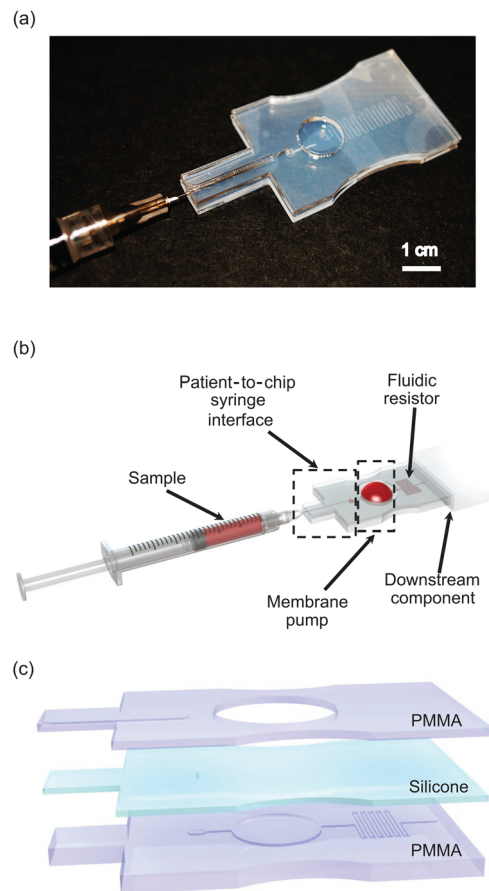


FIG. 1. (a) Image of the device with syringe and needle inserted. (b) Solid model of the device with all interconnected components: patient-to-chip syringe interface, membrane pump, fluidic resistor, and downstream component. An operator injects the patient sample into the device using the collection syringe directly. The sample is fully contained within the membrane pump, which inflates under the fluid pressure. Subsequently, the pump deflates and pushes the sample downstream, as regulated by the membrane characteristics and the fluidic resistor. (c) Exploded view of the device showing the PMMA and silicone layers. The top PMMA layer is 1.5 mm thick, the silicone layer is 1.6 mm thick, and the bottom PMMA layer is 3.0 mm thick.

pressure indicates both (1) the need to isolate the operator from the downstream processes, and (2) the relatively large potential for mechanical work in the syringe injection process. The membrane pump is designed to separate the operator from downstream components such that subsequent flow is not dictated by the operator's injection rate or hand strength. Instead, the fluid flow is controlled through prior engineering of the membrane pump's pumping capacitance and the downstream fluidic resistance of the fluidic resistor.

A. Patient-to-chip syringe interface

The syringe and needle is the standard accepted method of collecting ml-scale volumes of patient blood. The device components connecting the syringe and needle to the chip consist of a silicone seal, guiding channel for the needle, and check valve, as shown in Fig. 2(a). During sample injection into the device, the needle punctures the silicone seal and follows the guiding channel until it reaches the valve chamber. The guiding channel can be designed to accommodate any common needle length or diameter. After safely collecting the sample, the syringe can be unscrewed with the needle remaining in the chip for integrated sharps disposal. The check valve simply prevents sample backflow through the syringe interface following sample injection, as demonstrated previously with a membrane hole valve design.²⁴ As shown in Fig. 2(b), the through hole of the check valve lies within the silicone layer and only opens when there is

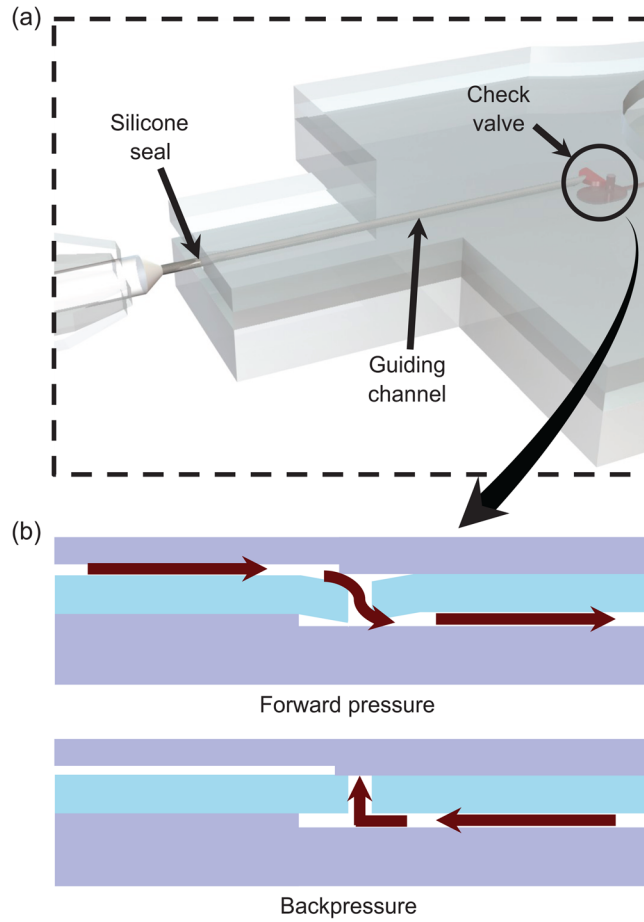


FIG. 2. Patient-to-chip syringe interface. (a) Magnified view showing the silicone seal, guiding channel for the needle, and check valve. (b) Schematic of the simple check valve enabled by the layered membrane pump design (open under forward pressure and closed under backpressure).

sufficient forward pressure in the valve chamber pushing against the silicone. Backpressure from the membrane pump closes the check valve (Fig. 2(b)).

B. Membrane pump

The membrane elastically deforms and stores sample volume as it is injected into the device, as shown in Fig. 3(a). The volume stored under a deflected membrane is defined by the spherical cap equation

$$V = \frac{\pi\delta}{6}(3r^2 + \delta^2), \quad (1)$$

where V is the stored volume, r is the radius of the membrane pump, and δ is the deflection of the membrane. The deflection of the membrane can be modeled analytically using solid mechanics theory for the deformation of circular, reservoir-bound elastic membranes.^{25–27} It is a function of the geometry of the reservoir and membrane, the material properties of the membrane, and the applied fluid pressure

$$\delta = \left(\frac{3r^4}{16Eh^3} \right) (1 - \nu^2)p, \quad \text{for } \delta \leq h, \text{ (linear regime)}, \quad (2)$$

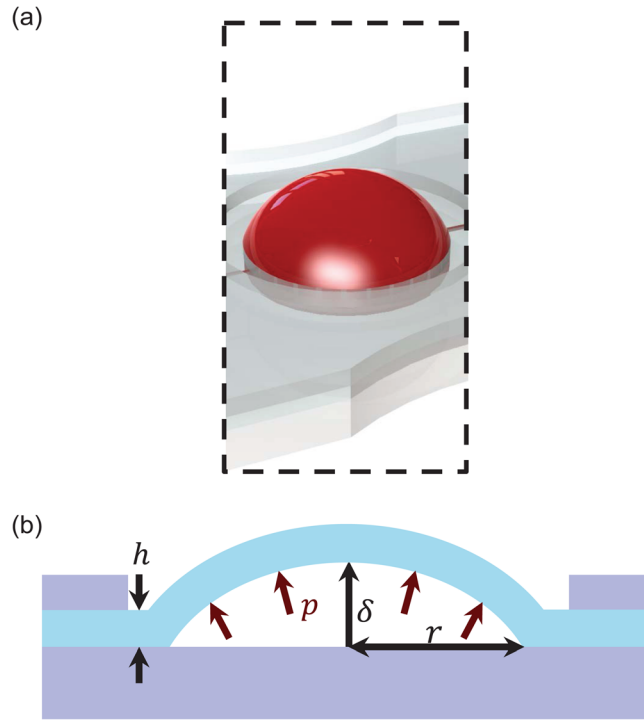


FIG. 3. Membrane pump. (a) Magnified view showing stored sample volume. (b) Schematic of the membrane pump inflated under fluid pressure.

$$\delta = h \left(\frac{3r^4(1-\nu)}{8Eh^4} \right)^{\frac{1}{3}}, \quad \text{for } \delta > h, \text{ (nonlinear regime)}, \quad (3)$$

where h is the membrane thickness, E is the elastic modulus of the membrane material, ν is the Poisson's ratio of the membrane material, and p is the applied fluid pressure, as shown schematically in Fig. 3(b). The Poisson's ratio for silicone elastomer is 0.5,²⁵ such that Eqs. (2) and (3) become

$$\delta = \left(\frac{9r^4}{64Eh^3} \right) p, \quad \text{for } \delta \leq h, \text{ (linear regime)}, \quad (4)$$

$$\delta = h \left(\frac{3r^4}{16Eh^4} \right)^{\frac{1}{3}} p^{\frac{1}{3}}, \quad \text{for } \delta > h, \text{ (nonlinear regime)}. \quad (5)$$

Deflection behavior is linear for $\delta \leq h$ and nonlinear for $\delta > h$ with respect to applied fluid pressure. It is noted that these equations hold only when the diameter of the membrane pump is much greater than the membrane thickness, $2r \gg h$, a condition that is met by the pump developed here.

C. Pump characterization through an electrical circuit analogy

Connecting a fluidic resistor to the membrane pump allows for controlled flow of stored sample volume to downstream components. The flow of the sample volume is dictated by the total resistance of the fluidic resistor and downstream components as well as the fluid pressure in the membrane pump which changes with time. In terms of an electrical circuit analogy, the membrane pump with the fluidic resistor and downstream components form a resistor-capacitor (RC) circuit, where the membrane pump serves as a capacitor. The pressure and flow rate

outputs from this fluidic RC circuit after loading can be defined by equivalent voltage and current output expressions for the electric RC circuit. These expressions are given as

$$p = p_o e^{-t/\tau}, \quad (6)$$

$$Q = \frac{p_o}{R} e^{-t/\tau}, \quad (7)$$

$$\tau = RC, \quad (8)$$

where p_o is the initial pressure in the membrane pump after loading, Q is the flow rate output at time t , τ is the characteristic time constant which governs the rate of decay in pressure and flow rate outputs, R is the total resistance of the fluidic resistor and downstream components, and C is the capacitance of the membrane pump. The capacitance is the derivative of the volume stored in the pump with respect to the applied pressure.²⁸ From this relationship, linear and nonlinear expressions for the pumping capacitance can be derived using Eqs. (1), (4), and (5)

$$C = \frac{\partial V}{\partial p} = \left(\frac{3\pi}{8k} \right) \left[\left(\frac{3p}{4k} \right)^2 + r^2 \right], \quad \text{for } \delta \leq h, \text{ (linear regime),} \quad (9)$$

$$C = \frac{\pi}{6} \left(\frac{h^2}{k} \right)^{\frac{1}{3}} \left[r^2 p^{-\frac{2}{3}} + \left(\frac{h^2}{k} \right)^3 \right], \quad \text{for } \delta > h, \text{ (nonlinear regime),} \quad (10)$$

$$k = \frac{16Eh^3}{3r^4}, \quad (11)$$

where k is the stiffness of the membrane (i.e., pressure required per unit deflection of the membrane center-point).²⁸ The pump outputs become increasingly more steady as τ is increased. Increasing τ by increasing capacitance, C , can be achieved by enlarging the pump (i.e., increasing pump radius) and/or connecting multiple pumps in parallel. The total resistance of the fluidic circuit, R , can also be increased; however, this approach reduces flow rate, and may or may not be suitable for a given application. In summary, combinations of pumps and pump geometry can be tuned in a straightforward manner to engineer pump performance. Pumping capacitance, C , is a particularly useful metric indicating the volume output available at a given pressure.

III. EXPERIMENTAL

A. Device fabrication

The device was fabricated from several layers of poly(methyl methacrylate) (PMMA) and silicone, as shown in Fig. 1(b). Both PMMA and silicone are biocompatible, inexpensive in bulk, and easy to fabricate, which greatly reduces the total material and fabrication costs of the device. Based on the current prices of PMMA and silicone (McMaster Carr, Aurora, OH, US; Plastic World, Toronto, ON, Canada), and a typical chip size (with an area of $60 \times 60 \text{ mm}^2$ per layer), the total material cost is ~ 0.20 USD/device.

The features of the device (e.g., channels, reservoirs, through holes) were micromachined into the PMMA and silicone layers via a CO_2 laser ablation system (Universal Laser Systems Inc., Scottsdale, AZ, USA). After micromachining, the PMMA layers were lightly polished with sandpaper to remove ablated residue, followed by cleaning in an ultrasonic bath (Thermo Fisher Scientific Inc., Waltham, MA, USA) for 15 min. The silicone layer was rinsed with deionized (DI) water and isopropanol to remove residue from the laser ablation. The bonding of the PMMA and silicone layers was based on the protocol provided by Kim *et al.*,²⁹ and we briefly summarize the steps here: (1) prepare a 5% v/v aqueous solution of (3-Aminopropyl)trimethoxysilane (APTMS) (Sigma-Aldrich Co. LLC., St. Louis, MO, USA) and heat to 85°C , (2) expose surfaces

of the PMMA layers to oxygen plasma for 1 min and immediately immerse in the heated APTMS solution for 30 min, (3) remove the treated PMMA layers and dry with compressed air, and (4) expose each side of the silicone layer to oxygen plasma for 1 min and sandwich between the treated PMMA layers in a heated press (Carver Inc., Wabash, IN, USA) at 85 °C under 1300 N for 60 min. The resulting device had a tensile bonding strength of about 1000 kPa.²⁹

B. Characterization of membrane pump

The pressure and flow rate outputs of a single membrane pump and multiple pumps connected in parallel were characterized using an experimental setup consisting of a syringe pump, pressure gauge, valves, and an analytical balance, as shown in Fig. 4. The membrane pump(s) was evaluated for both DI water and undiluted, anticoagulated, mouse whole blood (Cedarlane Laboratories Ltd., Burlington, ON, Canada). The mouse whole blood was used within 3 days upon reception as advised by the supplier. Fluid was injected by the syringe pump into the device via an on-chip port directly after the first valve as shown in Fig. 4. Flow was then directed to the membrane pump(s) through on-chip fluidic channels, where in the case of multiple pumps connected in parallel the network was filled simultaneously. It is important to note that the multiple pumps within the chip do not require additional input from the operator; these pumps are connected by the fluidic channels. This inflated the pump(s) to an initial gauge pressure of ~ 1 atm (103.4 kPa), and then upstream and downstream connections were closed to maintain that pressure (Fig. 4). After initially opening the downstream valve to allow flow, the valve was closed at fixed time intervals of 0.5, 1, and 2 min to collect and measure the mass output using the analytical balance. A volume output was calculated from the mass output using the density of the fluid (i.e., 1.0 g/ml for water and 1.1 g/ml for mouse whole blood). The volume output is the time-integral of the flow rate in Eq. (7). This relationship was used to calculate the characteristic time constant, τ , of the fluidic circuit. In Eq. (7), the total resistance, R , and time constant, τ , are the only unknown variables given that the initial pressure, p_o , was set to ~ 1 atm, which necessitates a system of two equations. The measured volume output at the three time intervals (0.5, 1, and 2 min) provided a system of three equations, where two equations were used to calculate τ and the third was used as verification. The capacitance of the pump was determined using Eq. (9) given the material properties and geometry of the membrane pump. Using this capacitance value and the calculated time constant, the total resistance, R , was ascertained using Eq. (8).

The pump pressure decay was measured directly; however, the results were unreliable due to instrumental error. Specifically, the pressure gauge contained a dead volume and a deformable diaphragm that acted as a pump with capacitance similar to the membrane pump. The result was experiments that overestimated the pumping capacitance significantly. For this reason, the gauge was closed off and the volume measurement approach was applied without real-time pressure measurement. Instead, pressure and flow rate outputs were calculated and plotted from the measured volume output of the pumps through Eqs. (6) and (7).

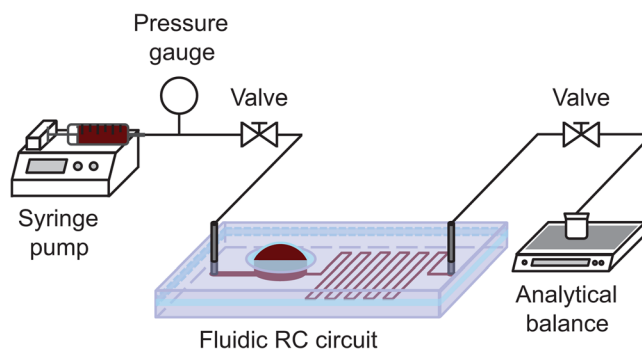


FIG. 4. Experimental setup used to determine the characteristic time constant of the fluidic RC circuit (shown magnified in the current view).

Red blood cell (RBC) lysis in the mouse whole blood was also investigated. Whole blood samples were observed with bright-field microscopy prior to and after pumping, which provided a rough estimate of RBC density. Shear stress in the device during flow was also calculated and compared to existing values required for lysing red blood cells.

IV. RESULTS AND DISCUSSION

A. Linear versus nonlinear pump deflection

Linear pump deflection behavior is generally preferred over nonlinear behavior (as described in Eqs. (4), (5), and (9)–(11)), particularly where transport can influence downstream diagnostics. The pumping capacitance for linear and nonlinear deflections was plotted against applied pressure for given pump geometry and material properties, as shown in Fig. 5, using Eqs. (9)–(11). The plot illustrates that the capacitance steadily increases in the linear deflection regime; however, it drops sharply at a transition pressure (p_t) when the deflection shifts to the nonlinear regime. This transition pressure decreases with increasing pump radius for fixed membrane thickness. The lowered pumping capacitance for nonlinear deflection effectively shortens the characteristic time of the fluidic circuit and thus decreases the steadiness of sample flow. For this reason, the membrane pump was designed such that linearity was maintained up to the applied working pressure of ~ 1 atm.

Different thicknesses of the silicone layer were employed to experimentally test the linearity of the membrane pump. Figure 6 shows the deflection-pressure relationship of the membrane pump for the two different membrane thicknesses, 0.5 mm and 1.6 mm, at a fixed pump radius of 2.5 mm. The solid and dashed lines in Fig. 6 are curve fits of the experimental data. For applied pressures up to 103.4 kPa and greater, the deflection of the thicker 1.6 mm membrane remained linear, while the thinner 0.5 mm membrane showed nonlinear behavior beyond $\delta = h = 0.5$ mm, as predicted by the theory. The 1.6 mm thickness for the silicone layer, which showed linear behavior throughout the range, was used for all subsequent experimental characterization.

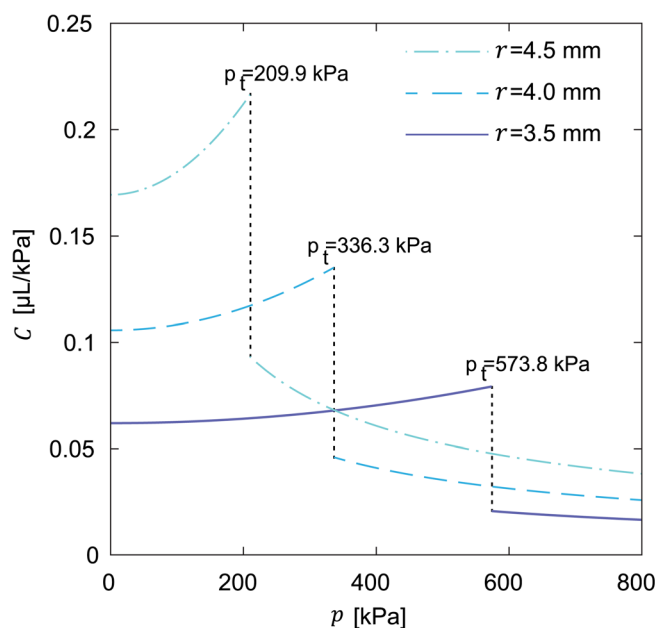


FIG. 5. Pumping capacitance for linear and nonlinear deflections. The capacitance steadily increases when deflection is linear, however, it drops sharply at a transition pressure (p_t) as the deflection becomes nonlinear. For different pump radii (3.5 mm (solid), 4.0 mm (dashed), and 4.5 mm (dotted-dashed)) at a fixed membrane thickness of 1.6 mm and elastic modulus of 1600 kPa, the transition pressure decreases with increasing radius. The transition pressures for each pump are indicated in the figure.

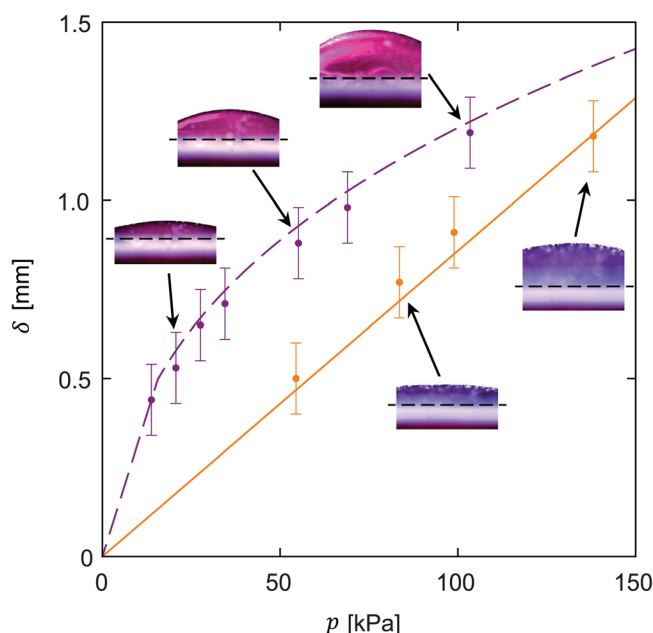


FIG. 6. Deflection-pressure relationship of the membrane pump for two different membrane thicknesses, 0.5 mm (dashed) and 1.6 mm (solid), at a fixed pump radius of 2.5 mm. For the 0.5 mm thick membrane, linear deflection transitions to non-linear deflection beyond $\delta = 0.5$ mm, while there is no transition for the 1.6 mm thick membrane. The inset images show the central portion of the pumps as viewed from the side at 20.7 kPa, 55.2 kPa, and 103.4 kPa for the 0.5 mm thick membrane (left), and at 83.6 kPa and 138.1 kPa for the 1.6 mm thick membrane (right). The dashed lines indicate the base of the spherical cap.

An upper bound on the pump radius was calculated using Eq. (4) to ensure the deflection of the membrane pump remained linear up to the applied pressure. The applied pressure was set to ~ 1 atm (103.4 kPa), and the maximum deflection was set equal to the membrane thickness (1.6 mm) to maintain linear deflection. The hardness of the silicone, as quantified by the shore durometer, was 40 A (McMaster Carr), which correlates to an elastic modulus of ~ 1600 kPa.³⁰ Solving Eq. (4) using these defined parameters yielded an upper bound of 4.8 mm for the pump radius.

B. Material delamination

Material delamination can lead to leakage and discrepancies in the sample flow. To prevent delamination while maintaining linear deflection, we calculated a lower bound on the pump radius using Eq. (4). The delamination pressure was 1000 kPa (i.e., tensile bonding strength of PMMA and silicone layers²⁹), the maximum linear deflection was the thickness of the membrane (1.6 mm), and the elastic modulus was 1600 kPa, which yielded a lower bound of 2.7 mm on the pump radius. Taking into consideration both the lower and upper bounds on the pump radius, 2.7 mm and 4.8 mm, a radius value of 4.5 mm was selected for subsequent testing to maximize the volume throughput while maintaining linearity.

C. Measurements of pumping pressure and flow rate

Pump performance as governed by the characteristic time constant, $\tau = RC$ (Eq. (8)), was measured and characterized by: (1) varying the total resistance, R , of the downstream fluidic circuit at a fixed capacitance, and (2) varying the total capacitance at a fixed resistance for both DI water and undiluted, anticoagulated mouse whole blood. Figure 7 shows the pressure and flow rate outputs of the membrane pump becoming more steady as the fluidic resistance increases, and this is shown quantitatively by the increase in the characteristic time constant from 21 to 63 s for water and from 53 to 97 s for whole blood from small to large fluidic resistor, respectively. However,

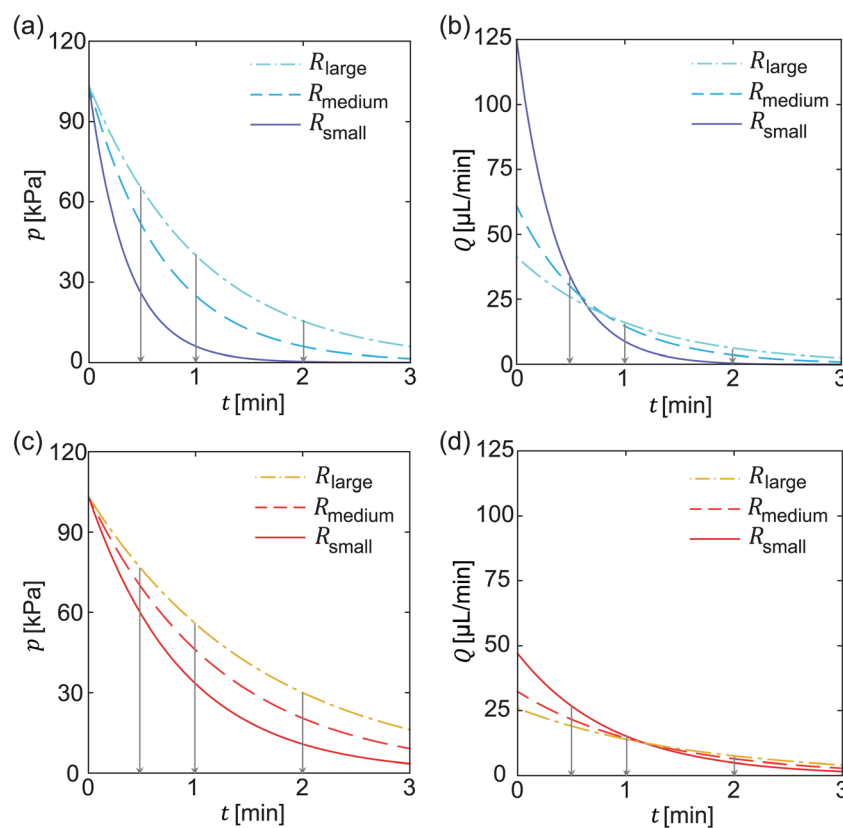


FIG. 7. Comparison of pressure and flow rate outputs for DI water and mouse whole blood for different total fluidic resistances. (a) Pressure and (b) flow rate outputs of the membrane pump for DI water for three different fluidic resistors: small (solid), medium (dashed), and large (dotted-dashed) with total resistances of 0.8 kPa min/ μ L, 1.7 kPa min/ μ L, and 2.5 kPa min/ μ L, respectively. The characteristic time constants of the small, medium, and large fluidic circuits were 21 s, 42 s, and 63 s, respectively, with a fixed total capacitance of 0.4 μ L/kPa. (c) Pressure and (d) flow rate outputs for mouse whole blood using the same three devices as for DI water. The high viscosity and hematocrit of the whole blood increased the total resistances to 2.2 kPa min/ μ L, 3.2 kPa min/ μ L, and 4.0 kPa min/ μ L, resulting in time constants of 53 s, 74 s, and 97 s for small, medium, and large resistors, respectively. The characteristic time constants were calculated using volume outputs at time intervals of 0.5 min, 1 min, and 2 min (as indicated by arrows) given the volume is the time-integral of the flow rate.

increasing the total resistance while fixing the total pumping capacitance and volume capacity greatly reduces the sample volume throughput (e.g., reduction in initial flow rate from about 125 μ L/min to about 40 μ L/min for water and from about 50 μ L/min to about 25 μ L/min for whole blood from small to large fluidic resistor, respectively). The flow rate also becomes more steady as the viscosity of the pumped fluid increases. The high viscosity and hematocrit of the whole blood increased the total resistance of the devices although the dimensions of the channels and downstream connections remained the same. The induced high resistance is related to the shear rate in the channels, where at low shear rates the viscosity of the whole blood appears to be higher than it would be at high shear rates.³¹ This property of blood flow can be leveraged to even out the flow rate output produced by the membrane pump. Although the form of the pressure/flow rate decay will in general be as shown in Fig. 7, required flow rates and total downstream fluidic resistance (including diagnostic channels) will be application specific.

For a fixed downstream fluidic resistance, pumping capacitance and volume capacity can be increased by connecting multiple membrane pumps in parallel. This approach was used rather than enlarging a single pump (i.e., increasing pump radius) to maintain linearity for each pump in the network (for membrane thickness, $h = 1.6$ mm and maximum pump radius, $r_{max} = 4.8$ mm). Enlarging a single pump decreases the transition pressure at which the pumping capacitance drops (Fig. 5). Figure 8 shows that the pressure and flow rate outputs become more steady without any decrease in initial throughput as more membrane pumps are added to the

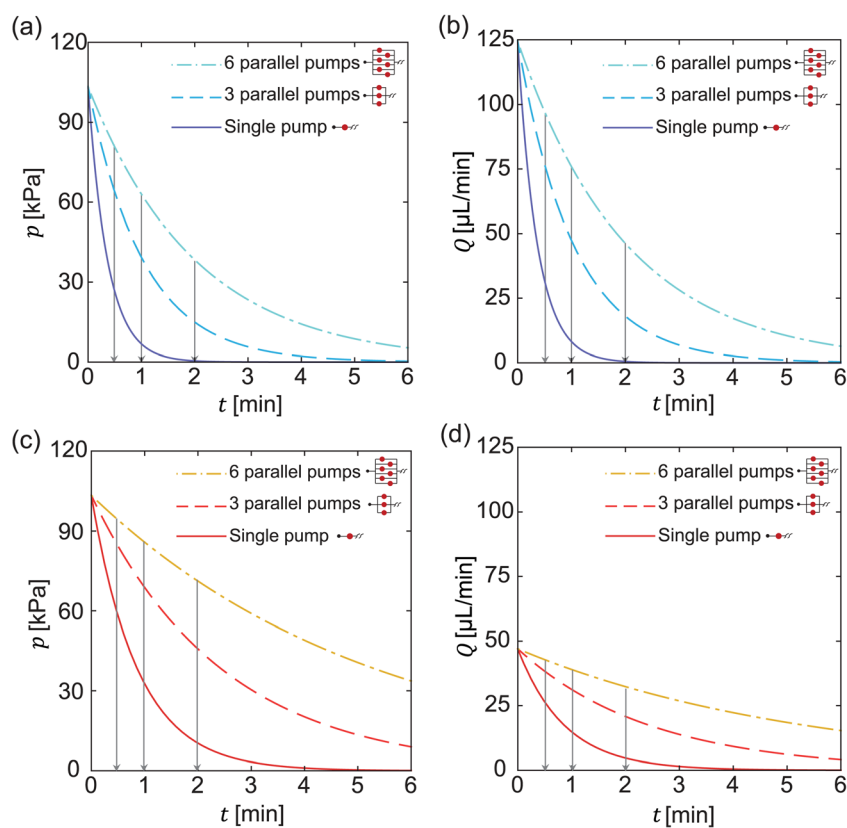


FIG. 8. Comparison of pressure and flow rate outputs for DI water and mouse whole blood for different total pumping capacitances. (a) Pressure and (b) flow rate outputs of the membrane pump for a single pump (solid), three pumps in parallel (dashed), and six pumps in parallel (dotted-dashed) with total capacitances of $0.4 \mu\text{L/kPa}$, $1.2 \mu\text{L/kPa}$, and $2.4 \mu\text{L/kPa}$, respectively. The characteristic time constants for the single, three, and six pumps in parallel are 22 s, 62 s, and 121 s, respectively, at a fixed total resistance of $0.8 \text{ kPa min}/\mu\text{L}$. (c) Pressure and (d) flow rate outputs for mouse whole blood using the same three devices as for DI water. The high viscosity and hematocrit of the whole blood increased the total resistance to $2.2 \text{ kPa min}/\mu\text{L}$ for the same total capacitances, resulting in time constants of 52 s, 147 s, and 321 s for the single pump, three pumps in parallel, and six pumps in parallel, respectively. The characteristic time constants were calculated using volume outputs at time intervals of 0.5 min, 1 min, and 2 min (as indicated by arrows) given the volume is the time-integral of the flow rate. The pump networks are shown schematically in the figure.

parallel network. For water, the measured characteristic time constant increases from 22 to 121 s from the single pump to six pumps in parallel, respectively, and the volume output increases from about 40 to $240 \mu\text{L}$. Similarly for whole blood, the characteristic time constant increases from 52 to 321 s from the single pump to six pumps in parallel, respectively, while having the same volume output as water. The observed linear scaling of the characteristic time constant is consistent with theory. The multiple membrane pump strategy thus provides a simple yet powerful way to scale the throughput of the device and enhance the flow control at the same time.

Whole blood samples before and after pumping were viewed under bright-field microscopy for the highest initial flow rates (i.e., small resistor and six pumps in parallel having initial flow rates of about $50 \mu\text{L/min}$). For both cases, there were minimal differences in the cell density of blood samples before and after pumping. The maximum shear stress in the devices is $\sim 8 \text{ Pa}$ given the maximum initial flow rate of $50 \mu\text{L/min}$, the cross-sectional area of the channels ($\sim 0.02 \text{ mm}^2$), the hydraulic diameter of the channels ($\sim 0.22 \text{ mm}$), and the viscosity of the mouse whole blood ($\sim 5 \text{ mPa s}$).³² This value is much lower than the shear stress required to lyse RBC's, 100 Pa .³³ Therefore, the membrane pump is capable of delivering viable cells (and plasma or sera) downstream for cell-based testing and analysis.

In contrast to existing on-chip pumping mechanisms,^{19,20} the membrane pump can provide larger sample volume and higher sample volume throughput for downstream analysis. Specifically,

up to 240 μl and about 25 $\mu\text{l}/\text{min}$ after 3 min of operation for both DI water and mouse whole blood (Figs. 8(b) and 8(d)) as compared to previous on-chip pumping methods with sample volume of $\sim 5 \mu\text{l}$ and a maximum flow rate on the order of 10 $\mu\text{l}/\text{min}$. The flow rate output of the membrane pump is also comparable to those of the electrically and pneumatically actuated pumps having maximum flow rates ranging from 10 $\mu\text{l}/\text{min}$ to several ml/min.^{10,34} The output here, however, is generated without any electric power or air supply requirements, which makes the device more suited to point-of-care applications in developing settings. The price for this all-mechanical operation is variability in output flow rate over time. As demonstrated here, this variability can be tuned through engineering resistance and particularly pump capacitance, while maintaining operation within the linear deflection regime.

V. CONCLUSIONS

A device consisting of an on-chip hand-powered membrane pump using a robust patient-to-chip syringe interface was presented. This strategy offers safe sample collection, sample confinement, integrated sharps disposal, and controlled sample volume throughput. The membrane pump captures the operator's mechanical work and delivers fluid to downstream components in a controlled manner. The maximum flow rate output of the membrane pump was comparable to those of electrically and pneumatically actuated pumps, with the advantage of no electrical power or air supply requirements. The pumping capacitance and volume capacity of the membrane pump was scaled by connecting multiple pumps in parallel. Our approach demonstrated higher sample volume throughput over existing on-chip pumping mechanisms. We anticipate the application of this device to point-of-care applications requiring biologically safe pumping mechanisms in developing settings, exploiting a readily available power source: the human hand.

ACKNOWLEDGMENTS

The authors gratefully acknowledge Grand Challenges Canada for financially supporting this project (Grant No. 0005-02-02-01-01), and the staff at the National Hospital for Tropical Diseases in Hanoi, Vietnam for their assistance and support. The authors also gratefully acknowledge infrastructure funding from the Canada Foundation for Innovation (CFI) and on-going support from the Natural Sciences and Engineering Research Council of Canada (NSERC).

- ¹G. M. Whitesides, *Nature* **442**, 368 (2006).
- ²M. M. Teymoori and E. Abbaspour-Sani, *Sens. Actuators, A* **117**, 222 (2005).
- ³K. Junwu, Y. Zhigang, P. Taijiang, C. Guangming, and W. Boda, *Sens. Actuators, A* **121**, 156 (2005).
- ⁴B. Ma, S. Liu, Z. Gan, G. Liu, X. Cai, H. Zhang, and Z. Yang, *Microfluid. Nanofluid.* **2**, 417 (2006).
- ⁵S. S. Wang, X. Y. Huang, and C. Yang, *Microfluid. Nanofluid.* **8**, 549 (2010).
- ⁶T. R. Pan, S. J. McDonald, E. M. Kai, and B. Ziaie, *J. Micromech. Microeng.* **15**, 1021 (2005).
- ⁷C. Yamahata, C. Lotto, E. Al-Assaf, and M. A. M. Gijis, *Microfluid. Nanofluid.* **1**, 197 (2005).
- ⁸A. Brask, D. Snakenborg, J. P. Kutter, and H. Bruus, *Lab Chip* **6**, 280 (2006).
- ⁹J. Rupp, M. Schmidt, S. Münch, M. Cavalar, U. Steller, J. Steigert, M. Stumber, C. Dorrer, P. Rothacher, R. Zengerle, and M. Daub, *Lab Chip* **12**, 1384 (2012).
- ¹⁰F. Amirouche, Y. Zhou, and T. Johnson, *Microsyst. Technol.* **15**, 647 (2009).
- ¹¹P. Yager, G. J. Domingo, and J. Gerdes, *Annu. Rev. Biomed. Eng.* **10**, 107 (2008).
- ¹²V. Gubala, L. F. Harris, A. J. Ricco, M. X. Tan, and D. E. Williams, *Anal. Chem.* **84**, 487 (2012).
- ¹³D. Erickson, D. Sinton, and D. Q. Li, *Lab Chip* **4**, 87 (2004).
- ¹⁴C. D. Chin, T. Laksanasopin, Y. K. Cheung, D. Steinmiller, V. Linder, H. Parsa, J. Wang, H. Moore, R. Rouse, G. Umvilighi, E. Karita, L. Mwambarangwe, S. L. Braunstein, d. W. van, R. Sahabo, J. E. Justman, W. El-Sadr, and S. K. Sia, *Nat. Med.* **17**, 1015 (2011).
- ¹⁵W. Li, T. Chen, Z. Chen, P. Fei, Z. Yu, Y. Pang, and Y. Huang, *Lab Chip* **12**, 1587 (2012).
- ¹⁶W. Wu, T. L. Kieu, and N. Y. Lee, *Analyst* **137**, 983 (2012).
- ¹⁷G. M. Walker and D. J. Beebe, *Lab Chip* **2**, 131 (2002).
- ¹⁸E. Berthier and D. J. Beebe, *Lab Chip* **7**, 1475 (2007).
- ¹⁹L. Gervais and E. Delamarche, *Lab Chip* **9**, 3330 (2009).
- ²⁰I. K. Dimov, L. Basabe-Desmonts, J. Garcia-Cordero, B. M. Ross, A. J. Ricco, and L. P. Lee, *Lab Chip* **11**, 845 (2011).
- ²¹G. Li, Y. Luo, Q. Chen, L. Liao, and J. Zhao, *Biomicrofluidics* **6**, 014118 (2012).
- ²²D. B. Weibel, A. C. Siegel, A. Lee, A. H. George, and G. M. Whitesides, *Lab Chip* **7**, 1832 (2007).
- ²³W. S. Yu, H. van Duinen, and S. C. Gandevia, *J. Neurophysiol.* **103**, 278 (2010).
- ²⁴S. Bohm, W. Olthuis, and P. Bergveld, *Sens. Actuators, A* **77**, 223 (1999).

- ²⁵*Handbook of Capillary and Microchip Electrophoresis and Associated Microtechniques*, edited by M. R. Begley, J. Monahan, and J. P. Landers (CRC, 2007), pp. 1121–1149.
- ²⁶M. Elwenspoek and R. Wierink, *Mechanical Microsensors* (Springer, 2001), pp. 80–81.
- ²⁷T.-R. Hsu, *MEMS and Microsystems* (John Wiley & Sons, Inc., 2008), pp. 112–113.
- ²⁸D. C. Leslie, C. J. Easley, E. Seker, J. M. Karlinsey, M. Utz, M. R. Begley, and J. P. Landers, *Nat. Phys.* **5**(3), 231 (2009).
- ²⁹K. Kim, S. W. Park, and S. S. Yang, *BioChip J.* **4**, 148 (2010).
- ³⁰A. N. Gent, *Trans. Proc. Inst. Rubber Ind.* **34**, 46 (1958).
- ³¹R. Wells and H. Schmid-Schönbein, *J. Appl. Physiol.* **27**, 213 (1969).
- ³²U. Windberger, A. Bartholovitsch, R. Plasenzotti, K. J. Korak, and G. Heinze, *Exp. Physiol.* **88**(3), 431 (2003).
- ³³A. M. Sallem and N. H. C. Huang, *Biorheology* **21**, 783 (1984).
- ³⁴D. J. Laser and J. G. Santiago, *J. Micromech. Microeng.* **14**, R35 (2004).